Size-Dependent Cellular Uptake and Expulsion of Single-Walled Carbon Nanotubes: Single Particle Tracking and a Generic Uptake Model for Nanoparticles

Hong Jin, Daniel A. Heller, Richa Sharma, and Michael S. Strano*

Department of Chemical Engineering, Massachusetts Institute of Technology, Building 66-566, 77 Massachusettes Avenue, Cambridge, Massachusetts 02139-4307

ABSTRACT The cellular uptake and expulsion rates of length-fractionated single-walled carbon nanotubes (SWNT) from 130 to 660 nm in NIH-3T3 cells were measured *via* single particle tracking of their intrinsic photoluminescence. We develop a quantitative model to correlate endocytosis rate with nanoparticle geometry that accurately describes this data set and also literature results for Au nanoparticles. The model asserts that nanoparticles cluster on the cell membrane to form a size sufficient to generate a large enough enthalpic contribution *via* receptor ligand interactions to overcome the elastic energy and entropic barriers associated with vesicle formation. Interestingly, the endocytosis rate constant of SWNT (10^{-3} min^{-1}) is found to be nearly 1000 times that of Au nanoparticles (10^{-6} min^{-1}) but the recycling (exocytosis) rate constants are similar in magnitude (10^{-4} to 10^{-3} min^{-1}) for poly(D,L-lactide-co-glycolide), SWNT, and Au nanoparticles across distinct cell lines. The total uptake of both SWNT and Au nanoparticles is maximal at a common radius of 25 nm when scaled using an effective capture dimension for membrane diffusion. The ability to understand and predict the cellular uptake of nanoparticles quantitatively should find utility in designing nanosystems with controlled toxicity, efficacy, and functionality.

KEYWORDS: single-walled carbon nanotubes (SWNT) · cellular uptake · endocytosis · exocytosis · nanoparticles · size-dependent uptake · endocytosis rate · single particle tracking (SPT)

Understanding the cellular internalization of nanoparticles[1−11] is a problem central to many emerging applications of biological nanotechnology. Such applications include the design of tissue-implantable or subcellular sensors,[12,13] drug-delivery systems,[14] and novel photodynamic therapies.[15] Nanoparticles of technological importance include functionalized carbon nanotubes,[3−10] Au,[1,2,16−18] and poly(D,L-lactide-co-glycolide; PLGA)[11] nanoparticles along with other types.[19] Cellular uptake of nanoparticles is found to involve endocytosis for the majority of cases.[1,2,6,7,9,10] Particularly for Au nanoparticles with a diameter of 14−100 nm[1,2] and DNA wrapped single-walled carbon nanotubes (DNA-SWNT) with lengths less than 1 μm,[7] the internalization mechanism is confirmed to be receptor-mediated endocytosis (RME).[20,21] The generic uptake mechanism arises from the adhesion of media proteins to the surfaces of nanoparticles during a typical cell culture incubation experiment,[1,4] as originally discussed by Lynch and co-workers in the literature.[22] Briefly, in most *in vivo* experiments, the nature of the nanoparticle surface is modified by the outermost protein layer of adsorbed proteins. The nature of this outer protein layer is considered to be the single most important parameter in determining the nanoparticle-cell interaction.

Theoretical progress has been made in understanding how the geometry of a nanoparticle can potentially influence its endocytosis rate. However a quantitative description remains elusive with some key aspects unexplained. Gao and co-workers[23] used a thermodynamic and mechanic analysis derived by Freund and Lin[24] to estimate the RME rate of a nanoparticle. Briefly, in the process of RME of nanoparticles, receptors binding to the curved nanoparticle surfaces causes membrane curvature with a corresponding increase in elastic energy. On the other hand, this receptor−ligand binding also causes configurational entropy to be reduced from the immobilization of the receptors. Meanwhile, receptors can diffuse to the wrapping site driven by the local reduction in free energy, allowing the complete membrane wrapping around the particle (endocytosis). Decuzzi and Ferrari[25,26] generalized this approach to include the

*Address correspondence to strano@mit.edu.

Received for review August 24, 2008 and accepted December 09, 2008.

Published online January 6, 2009.
10.1021/nn800532m CCC: $40.75

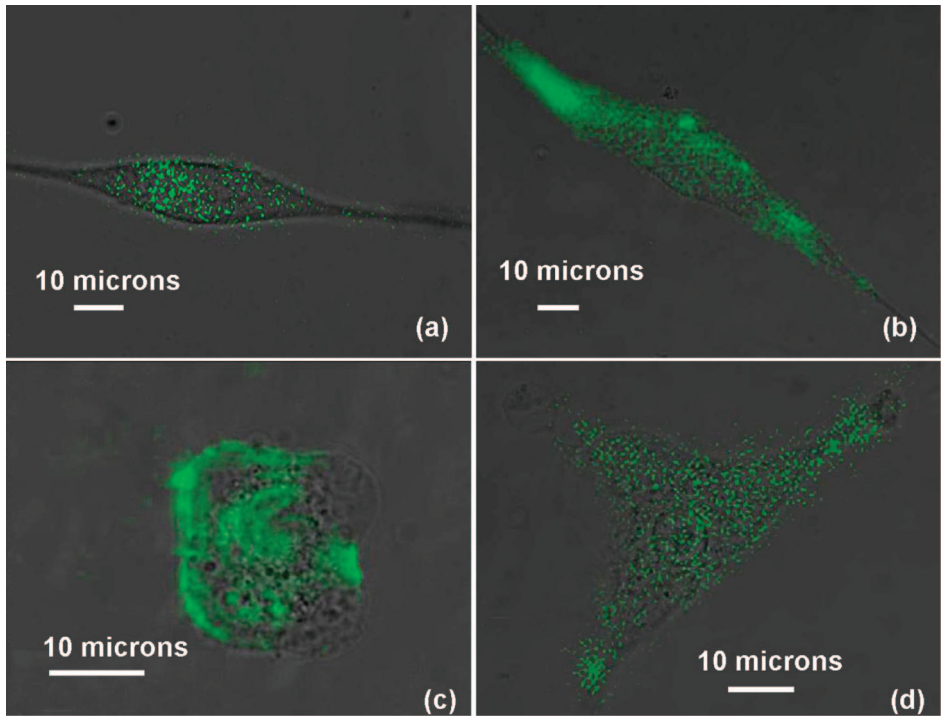

Figure 1. Colocalization of the fluorescence from SWNT (green) with its corresponding cell image at the final stage of the experiment for the four different lengths: (a) 660 ± 40, (b) 430 ± 35, (c) 320 ± 30, and (d) 130 ± 18 nm.

contribution of nonspecific forces such as electrostatics arising at the cell−nanoparticle interface. All existing models to date predict a threshold radius below which nanoparticle uptake by RME is impossible, and a highly asymmetric distribution of rates that decrease as nanoparticle diameter increases. Experimentally, the distribution is instead highly symmetric for both Au nanoparticles in the literature[1,2] and DNA-SWNT, as we have demonstrated for the first time in this work. Moreover, there is relatively little quantitative data or predictive modeling of the dynamics of nanoparticle trafficking into mammalian cells, despite significant progress in the quantitative description of endocytosis for small molecule ligands.[27,28]

In this work, we have developed the first quantitative model capable of relating the RME rate of spherical and anisotropic nanoparticles to their geometry and predict important aspects of their trafficking dynamics. We provide indirect evidence that nanoparticle surface clustering on the external cellular membrane facilitates RME by lowering the otherwise prohibitive thermodynamic barrier. The formalism explains why particles with a radius smaller than 25 nm can be endocytosed in this manner, a fact not explained by previously developed models. We validate the model experimentally for a GT repeating 30-nucleotide ($d(GT)_{15}$) wrapped SWNT of controlled lengths ranging from 130 ± 18 to 660 ± 40 nm and show that the mechanism accurately describes data for SWNT in this work and also for Au nanoparticles with diameters from 14 to 100 nm.[1,2] Also consistent with our model is the recent study which shows that the changes in nanoparticle size affect the binding capacity of antibody-coated Au nanoparticles with receptors.[29] The model is also the first to quantitatively describe the dynamics of nanoparticle uptake and trafficking, as we demonstrate for the aforementioned SWNT using single particle tracking (SPT). All three nanoparticle types (Au, SWNT, and PLGA) show that recycling (exocytosis) rate constants calculated from the model are similar in magnitude, which are more related to the membrane turnover rate constant.

DISCUSSION

Length-Dependent Uptake of DNA-SWNT. While size-dependent cellular uptake studies of spherical particles have been performed for citrate-coated Au nanoparticles,[1,2] these studies have not been fully explored for highly anisotropic particles after the first study of SWNT length and cellular uptake.[3] Chan and co-workers[1,2] reported that the maximum uptake in HeLa cells occurs with 50 nm diameter Au nanoparticles after a 6 h incubation.

We use $d(GT)_{15}$ wrapped SWNT with a high aspect ratio (see Methods) to directly study the length effect on cellular uptake using well-characterized platform employed in several of our previous studies[12,13,30,31] and others' studies.[7,32,33] To obtain the uptake for different lengths, we used an altered imaging optical microscope for SPT in the n-IR with a perfusion stage as described previously.[4] During a typical experiment, a steady flow of cell media, Dulbecco's Modified Eagle's Medium (DMEM), is established followed by a pulse of 0.025 mg of perfused DNA-SWNT in media. To compare the difference in the uptake, the concentration of SWNT (5 mg/L), the total volume of SWNT (5 mL), and the perfusion speed (5.65 μL/s) are kept constant. We note that the amount of SWNT for different lengths is magnitudes greater than the available receptors on the cell membrane so we could consider SWNT to be in excess. Because SWNTs do not photobleach, we are able to track their fluorescence trajectories relative to the cell for up to 6 h (Methods). Figure 1 shows the colocalization of the fluorescence of SWNT (green) with the cell image at the end of each experiment. As shown in the figure, long (Figure 1a, 660 ± 40 nm) and short (Figure 1d, 130 ± 18 nm) SWNTs have lower fluorescent intensities

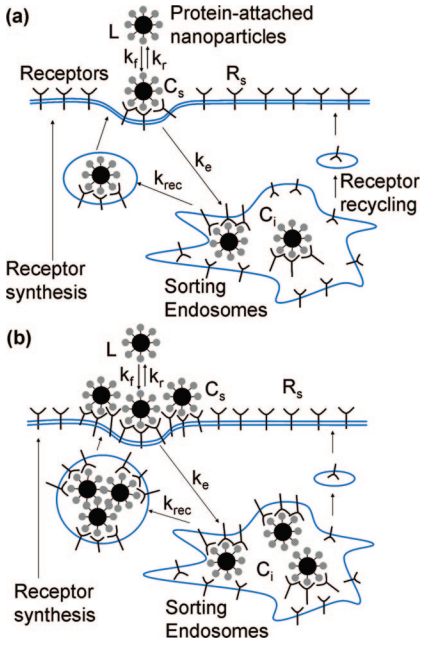

Figure 2. An illustration of endocytosis, trafficking and exocytosis steps in the model for (a) single nanoparticle and (b) nanoparticle clusters. Nanoparticles with an extracellular concentration of L can reversibly bind to free surface receptors (R_s) with binding and dissociation rate constant of k_f and k_r, respectively, and form nanoparticle-receptor complexes on the membrane with a concentration of C_s. These complexes can be endocytosed with a rate constant of k_e. A fraction of the internalized nanoparticle-receptor complexes (C_i) can be recycled back to the plasma membrane with a rate constant of k_{rec}. Other factors, such as the recycling and synthesis of the free receptors, do not affect L, C_i, and C_s and thus will not be discussed in this model.

than SWNTs with an average length of 430 ± 35 nm (Figure 1b) and 320 ± 30 nm (Figure 1c). The 320 nm length SWNTs have the highest uptake even if one corrects for the length dependent quantum yield. The SWNT quantum yield has been shown to increase with length.[31] If a correction is applied,[34] 320 nm remains the maximum.

From our previous work, the endocytosis and exocytosis are dynamically regulated for SWNTs,[4] and the corrected intensity therefore reflects only the accumulation difference for different lengths. The exocytosis rate can be decoupled from the nanoparticle net accumulation data *via* separate parallel experiments, as recently reported for Au nanoparticles.[2] Alternatively, the ability to track and compile statistics on a single SWNT in real-time allows for a direct measurement of the endocytosis rate using SPT. Briefly, trajectories of nonphotobleaching SWNT are extracted using ImageJ and the ParticleTracker plugin.[35] Endocytosis and exocytosis events are documented in real-time using a Matlab script.[4]

Size-Dependent Uptake Model for Nanoparticles. The rates of internalization and recycling of membrane receptor-bound low molecular weight ligands can be described by a variety of kinetic network models[27,28] that approximate the rate of transport between various cellular compartments. Experimental work has confirmed that such networks (Figure 2a) accurately predict the dynamics of cellular endocytosis of small molecules and proteins, the mechanism of which is not restricted to RME; however their application to nanoparticle trafficking has not yet been explored. In this work, we propose that nanoparticles bound to membrane receptors initially follow similar trafficking mechanisms (Figure 2b). Our interest is only in those pathways that dominate the observable rates of uptake and expulsion, and therefore we neglect less important details of the endocytosis process. The unbound, protein-coated nanoparticles of concentration, L, adsorb *via* cell membrane surface receptors of density R_s to the membrane with k_f and k_r as forward and reverse adsorption rate constants, respectively, creating a concentration C_s at the membrane surface. With rate constant k_e, the adsorbed particle can be internalized into an endosome with cellular concentration C_i. As we have demonstrated directly for the first time for SWNT,[4] in this scheme the nanoparticle either accumulates inside the cells or is recycled back to the membrane with rate constant k_{rec}. Membrane receptors are also recycled to the cell surface.

In our model, we assert that nanoparticles first reversibly adsorb to the plasma membrane and form receptor-bound complexes capable of membrane surface diffusion (Figure 2b). This process invariably causes clusters of sufficient size to lower the elastic energy required for wrapping so it can be overcome by the free energy reduction associated with receptor-particle binding, driving the diffusion of receptors for internalization[23−26] as detailed previously. This is consistent with the experimental data for SWNT in this work and those published previously for Au nanoparticles,[1,2]

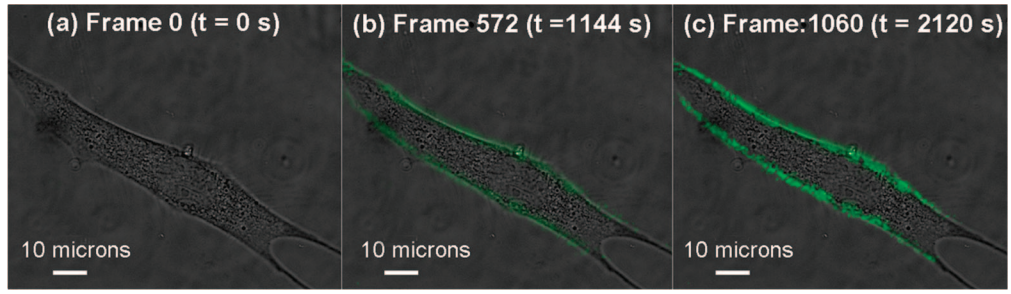

Figure 3. Experimental observation of SWNT surface clustering on the cell membrane (430 ± 35 nm SWNT is shown as an example). The fluorescence of SWNT indicated by green is projected onto the corresponding phase contrast image of the cell. (a) At the beginning of the experiment (t = 0 s), there is no SWNT present; (b) a thin layer of SWNT adsorption on the cell membrane is observed at t = 1144 s; (c) this layer becomes denser at t = 2120 s, indicating the existence of surface clustering.

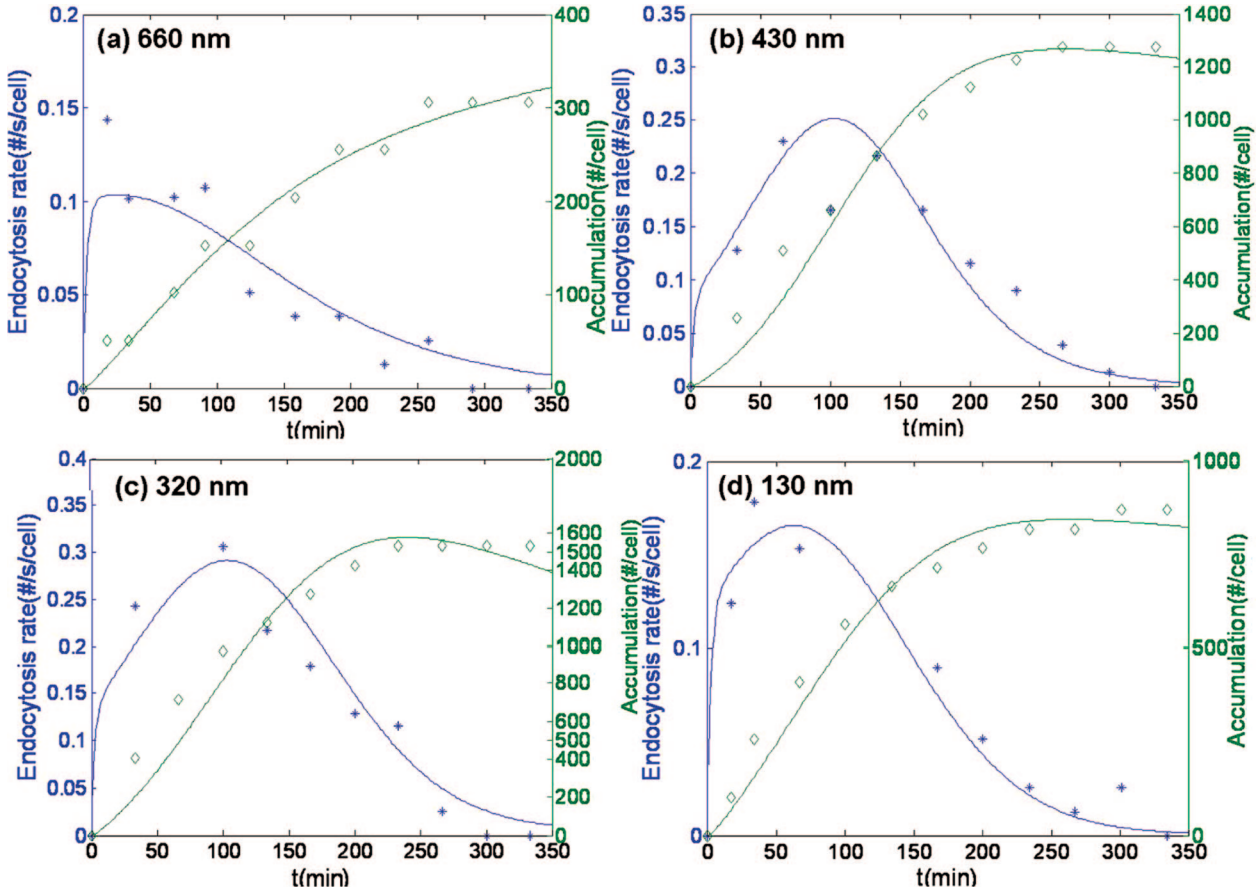

Figure 4. Endocytosis rate (number/s/cell, blue) and accumulation (number/cell, green) of DNA-SWNT complexes are solved numerically *via* eq A6 and eq A11 in real-time for SWNTs of length (a) 660 ± 40, (b) 430 ± 35, (c) 320 ± 30, and (d) 130 ± 18 nm, respectively. The endocytosis rate and accumulation data obtained by SPT is shown in blue diamonds and empty green diamonds. The results obtained using the parameter values of $k_a = 7 \times 10^{-4}$ min^{-1} and $k_r = 0.34$ min^{-1} are summarized in 1a.

where internalization of smaller particles far below the predicted threshold optimum is significant. Moreover, this assumption is also consistent with a distinct increase in near-infrared fluorescence from SWNT concentrated at the external cell membrane during the early stages of the transient uptake experiment (Figure 3). The illuminated exterior of the cell from adsorbed nanotubes is magnitudes higher than a single nanotube. To get this larger intensity, in a diffraction limited spot, it is highly possible that the nanotubes distribute or pack in a cluster.

The thermodynamic aspects of size-dependent RME have been addressed previously.[23,24] In this work, we instead focus on complex formation at the membrane surface in the following derivation. Consider two spherical nanoparticle complexes A and B in this process. The diffusion-controlled association rate constant is calculated to be [36,37]

$$k = 2\pi\lambda(D_A + D_B)(R_A + R_B) \quad (1)$$

where D_A and D_B are the surface diffusion constants for A and B respectively, R_A and R_B are the radii of particles A and B respectively. In eq 1, λ is calculated as[37]

$$\lambda = \frac{\gamma K_1(\gamma(R_A + R_B))}{K_0(\gamma(R_A + R_B))}$$

where γ is the inverse of half the average distance traveled by a reactant molecule in the time before desorption and K_0 and K_1 are the modified Bessel functions of the second kind.

For cylindrical molecules such as carbon nanotubes, ref 36 and 38 provide an effective capture radius R^* defined by

$$R^* = a / \ln(2a / b) \quad (2)$$

where a and b are the major and minor semiaxes of the cylinder.[36,38] Remarkably, when this effective capture radius is used for carbon nanotubes, their relative uptake becomes nearly identical to Au nanoparticles, indicating its importance as an effective scaling metric.

The extracellular nanoparticles can reversibly adsorb onto the membrane. Adsorbed complexes (protein-coated SWNT or protein-coated Au NP) diffuse on the cell membrane surface and form clusters with a radius of sufficient size that eventually satisfy the thermodynamic requirement for endocytosis.[23] This process is described as follows:

$$A(\text{extracellular}) \underset{k_{-1}}{\overset{k_1}{\rightleftharpoons}} A_1$$

$$A_1 + A_1 \underset{k_{-2}}{\overset{k_2}{\rightleftharpoons}} A_2$$

$$A_2 + A_1 \underset{k_{-3}}{\overset{k_3}{\rightleftharpoons}} A_3$$

$$A_3 + A_1 \underset{k_{-4}}{\overset{k_4}{\rightleftharpoons}} A_4$$

$$\cdots$$

$$A_i + A_1 \underset{k_{-(i+1)}}{\overset{k_{i+1}}{\rightleftharpoons}} A_{i+1}$$

$$A_i \underset{k_{rec}(Ri)}{\overset{k_{rec}(Ri)}{\rightleftharpoons}} (\text{endocytosed})$$

where A(extracellular) represents the nanoparticle in the bulk during experiments, A_1 represents single nanoparticle-receptor complex, and A_i represents a cluster formed by i such singlets. The endocytosis and recycling rate constant is represented by $k_e(R_i)$ and $k_{rec}(R_i)$ for clusters of radius R_i. We assume that the concentration of A_1 is constant because of the extracellular reservoir of A. The population of A_i changes according to

$$[A_1] \approx \text{constant}$$

$$\frac{d[A_i]}{dt} = k_i[A_1][A_{i-1}] + k_{-(i+1)}[A_{i+1}] + k_{rec}(R_i)[A_i(\text{endocytosed})] - (k_{i+1}\cdot[A_1]\cdot[A_i] + k_{-i}\cdot[A_i] + k_e(R_i)[A_i]) \quad \text{for } i = 2, 3, 4, \ldots$$

where $[A_i]$ is the concentration of A_i. The endocytosis and recycling process is much slower compared to the clustering process, so at early time,

$$\frac{d[A_i]}{dt} = k_i[A_1][A_{i-1}] + k_{-(i+1)}[A_{i+1}] - (k_{i+1}[A_1][A_i] + k_{-i}[A_i]) \quad \text{for } i = 2, 3, 4, \ldots$$

At the early stage of the clustering process, the clustering rate is much larger than the reverse rate, so

$$\frac{d[A_i]}{dt} = k_i[A_1][A_{i-1}] - k_{i+1}[A_1][A_i] \quad \text{for } i = 2, 3, 4, \ldots$$

As this process advances, pseudoequilibrium is reached for the clusters of radius R_i as long as larger clusters are permitted to form:

$$[A_i] = \frac{k_2}{k_{i+1}}[A_1] \quad \text{for } i = 2, 3, 4, \ldots$$

These assumptions simplify the problem mathematically and allow us to solve for $[A_i]$ given the complication of eq 1. The corresponding association rate constants are calculated as (*via* eq 1):

$$k_i = 2\pi\,\lambda(iR, \gamma)\,2DiR$$

Neglecting the small change in γ and knowing that $K_o(\gamma iR)/K_1(\gamma iR) \approx 1$, one obtains

$$[A_i] = \frac{2}{i+1}[A_1]$$

The total endocytosis rate can then be expressed as

$$r = \sum_{i=1}^{\infty}[A_i]k_e(R_i) = \sum_{i=1}^{\infty}\frac{2[A_1]}{i+1}\cdot k_e(R_i) \qquad (3)$$

or for the clusters of radius R_i, the endocytosis rate is

$$r_i = \frac{2[A_1]}{i+1}\cdot k_e(R_i)$$

Here, R_i represents the radius of the cluster formed by i singlets as shown in Supporting Informationi, Figure S1. We use the unmodified intrinsic endocytosis rate constant, k_e, from Gao and co-workers[23] to describe uptake of a cluster of radius R_i. It should be noted that eq 3 requires no additional parameter estimation and introduces only known or measurable parameters. Experimentally, the observed endocytosis rate constant can be obtained directly from transient nanoparticle uptake data as a function of time and incubation concentration as detailed in the Appendix for comparison and validation of eq 3.

DNA-SWNT. We model the dynamics of SWNT uptake quantitatively for the four different lengths in Figure 4 (see Methods and Appendix). As with Au nanoparticles in the literature,[1,2] there is a maximum rate observed except for SWNT, it occurs at 320 nm length. We note that the effective capture radius for SWNT of this size is 26.4 nm (*via* eq 2), which is very close to the 25 nm radius reported for maximum update of Au nanoparticles.[1,2] Further, our model describes the equilibrium cellular uptake as a function of the size for both Au nanoparticles and DNA-SWNT (Figure 5). The uptake of DNA-SWNT of different lengths is demonstrated in Figure 5a. The calculations for SWNT are shown in Figure 5b with contributions from clusters varying from singlets (A_1) to quintuplets (A_5) as example curves compared to the summation model distribution. As seen in Figure 5c, the model can accurately predict the experimental trends observed for the uptake of both Au nanoparticles and SWNT. Here, we have assumed a Gaussian distribution of energies for the nanoparticle-receptor bond (e_{RL}) and the excess binding energy (e_c) with a mean of 15(k_BT) for $e_{RL} + e_c$[23] and a standard deviation of 12(k_BT). The ratio ($\tilde{\xi}$) of the initial receptor density on the membrane to the receptor density at the nanoparticle−receptor contact area[23] was estimated at 0.01. In the SPT experiments, the initial SWNT concentration is 5 mg/L. The cell density is 1.4×10^{-4}

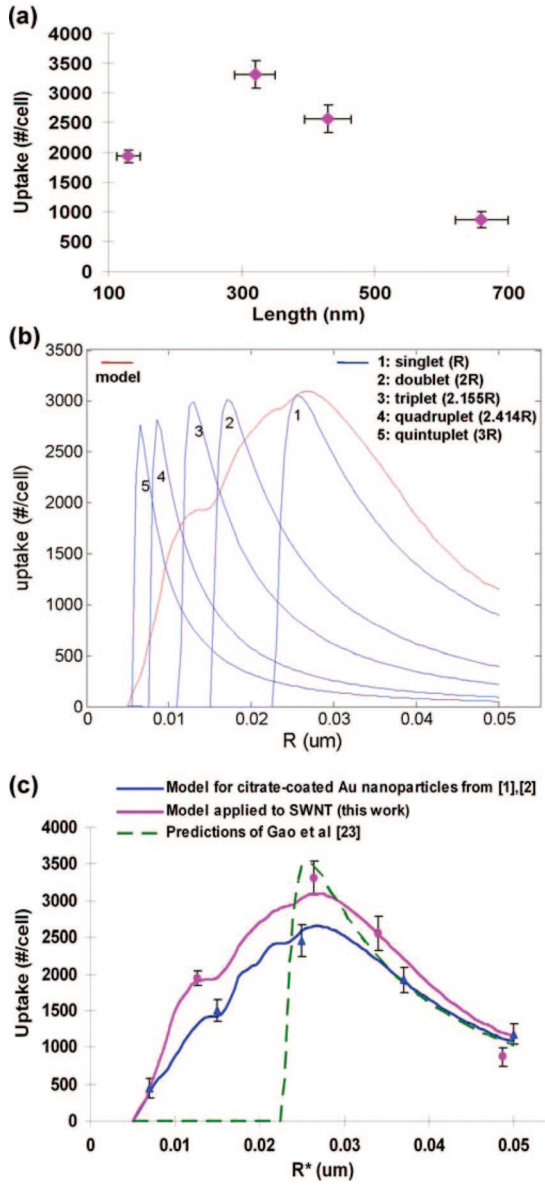

Figure 5. (a) The uptake of DNA-SWNT of different lengths obtained by SPT. (b) The symmetric size-dependent uptake curve (red) in this model (eq 3) is obtained by adding up the contributions from clusters of different sizes (singlets, doublets, triplets, *etc.*) shown in blue curves. The calculations of SWNT are shown here as an example. (c) The uptake of Au nanoparticles (blue) and DNA-SWNT (pink) of different sizes is described by the model eq 3 and compared to the model prediction in ref 23. The size R* for SWNT in this case can be scaled *via* eq 2 with the value for Au nanoparticles case remaining as the radius.

cells/μm^2, hence L_0 is 4.5×10^7/cell in eq A11. Values for k_r, and k_f depend on the type of ligand attached (intentionally or otherwise) to the nanoparticles and their corresponding receptors on the membrane. Both quantities can be estimated from the literature.[27] The estimates for k_r and k_f are 0.34 min^{-1} and 7.2×10^7 M^{-1} min^{-1}, respectively, and k_a is 7×10^{-4} min^{-1} from a receptor concentration of 10^5/cell and a cell density of 6×10^7 cell/L (eq A7). Our model is used to fit the cellular uptake quantitatively for SWNTs of different length and the results are shown in Figure 4 and 1a. The confidence interval is 95% throughout this work.

Au Nanoparticles. In eq A10, l_0 is the extracellular concentration of free nanoparticles at $t = 0$ and is estimated to be 10 uM,[1] that is, 10^7/cell given a confluent cell density of 10^{11} cells/L. The average estimate for k_r and k_f is 0.34 min^{-1} and 7.2×10^7 M^{-1} min^{-1}, respectively. Thus k_a can be estimated as 1.196 min^{-1} from a receptor concentration of 10^5/cell[27] and a cell density of 10^{11} cell/L (eq A7). Specifically when transferrin functions as the ligand, the estimate for k_r and k_f is 0.1 min^{-1} and 3×10^6 M^{-1} min^{-1}, respectively.[27] Transferrin receptor density is 5×10^4/cell so the calculated k_a is 0.025 min^{-1} (eq A7). Only two unknown parameters remain in eq A10, k_e and k_{rec}. They are obtained *via* nonlinear regression. The plot of Au nanoparticle uptake into HeLa cells *versus* time[1] is shown in Figure 6a. The fitting result is summarized in 1b.

The endocytosis rate constant is on the magnitude of 10^{-6} min^{-1}, with a maximum at a diameter of 50 nm, consistent with the experimental result. The recycling rate constant generally decreases with nanoparticle diameter, also in agreement with the experimental finding that the exocytosis of Au nanoparticles is linearly related to size, with particles of larger diameter less likely to be exocytosed.[2] The recycling rate constant of Au nanoparticles is larger than that of DNA-SWNT. This rate should depend upon cell type (Hela cell for Au nanoparticles in ref 1 and 2 and 3T3 cell for DNA-SWNT in this work) and nanoparticle properties and is closely related to the membrane turnover rate.

The size-dependent, steady-state cellular uptake of Au nanoparticles with serum protein and transferrin coatings are compared in the literature.[1] The uptake of transferrin-coated Au nanoparticles is found to have a similar trend as those coated with serum protein, with a maximum uptake at a diameter of 50 nm. However, the uptake of transferrin-coated Au nanoparticles is only $^1/_3$ that of the serum protein-coated ones. The result is consistent, since transferrin represents only one kind of protein in cell media and cells should display multiple receptor types, diminishing the surface density of transferrin-specific receptors.[39] As a result, transferrin-receptors are quickly saturated by the transferrin-coated Au nanoparticles while for serum-coated nanoparticles, the surface density of receptors is much larger, since many kinds of receptors are available. However, this does not necessarily mean that transferrin is less favored or has a smaller endocytosis rate. Setting $t \to \infty$ in A10, the endocytosis rate constant (k_e) can be compared for these two cases. As shown in 1c, for transferrin, k_e is larger for all diameters, and disproportionately larger for the 50 nm-diameter case. Transferrin is endocytosed *via* clathrin-mediated endocytosis[40] and the microcages of clathrin coats that nucleate near or at the edge of a region of a clathrin network are almost perfectly spherical, with a radius of ~25 to 30 nm.[41]

TABLE 1. Model Parameter Regression for the Endocytosis Rate Constant (k_e) and Recycling Rate Constant (k_{rec}) of (a) DNA−SWNT with Lengths from 130 to 660 nm, (b) Au Nanoparticles with Diameters of 14, 50, and 74 nm, (c) Au Nanoparticles with Diameters from 14 to 100 nm in Media (Serum Protein Coating) and in Transferrin (Transferrin Coating) and (d) PLGA Nanoparticles with a Diameter of 97 ± 3 nm.

		(a) DNA−SWNT (This Work)			
	130 ± 18 nm	320 ± 30 nm	430 ± 35 nm	660 ± 40 nm	
k_e ($\times 10^{-3}$ min^{-1})	13.6 ± 1.0	28.2 ± 1.9	17.7 ± 1.3	5.5 ± 0.4	
k_e (min^{-1})	0.0010 ± 0.0001	0.0008 ± 0.0001	0.0006 ± 0.0001	0.0002 ± 0.00003	
		(b) Au Nanoparticles[1]			
	14 nm	**50 nm**	**74 nm**		
k_e ($\times 10^{-6}$ min^{-1})	3.57 ± 0.76	4.53 ± 0.85	2.20 ± 0.34		
k_{rec} (min^{-1})	0.0069 ± 0.0020	0.0055 ± 0.0014	0.0054 ± 0.0012		
		(c) Au Nanoparticles [1]			
	14 nm	30 nm	50 nm	74 nm	100 nm
k_e ($\times 10^{-6}$ min^{-1}) media	2.61	3.45	4.21	2.76	1.14
k_e ($\times 10^{-6}$ min^{-1}) transferrin	2.76	3.83	5.91	3.44	8.75
k_{rec} (min^{-1}) both	0.0069	0.006	0.0055	0.0054	0.0050
		(d) PLGA Nanoparticles [11]			
k_e ($\times 10^{-4}$ min^{-1})	6.13 ± 1.07		k_e (min^{-1})	0.0073 ± 0.0020	

Poly(D,L-lactide-*co*-glycolide; PLGA) Nanoparticles. For PLGA nanoparticles with a diameter of 97 ± 3 nm, cellular uptake *versus* time, attributed to endocytosis, has been reported for human arterial vascular smooth muscle cells.[11] The results of nonlinear regression of k_e and k_{rec} using eq A10 are shown in Figure 6b and 1d.

While the endocytosis rate constant differs by a factor of 10^3 in all three cases, the recycling rate constant only varies by a factor of 10. The values of k_e found for the Au and PLGA nanoparticles are 4 orders of magnitude lower than constitutive membrane component turnover rate constants (0.01 min^{-1}),[42] which suggests that suppression of coated vesicle formation and/or uptake might be occurring in those situations. This suppression may be due to the nature of the nanoparticles or the interaction of the cell membrane with the nanoparticle. The values found for the SWNT are much more in line with typical constitutive membrane turnover and thus no or little suppression may exist. The recycling rate constant, on the other hand, is quite similar across cell lines and nanoparticles, which may primarily depend upon the membrane turnover rate. Many aspects are amenable to quantitative analysis in our model.

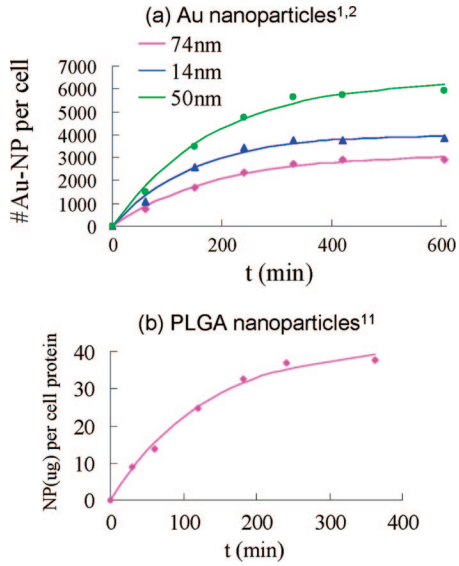

Figure 6. (a) Au nanoparticles of different diameters from ref 1 and 2: 14 nm (blue triangles), 50 nm (green circles), and 74 nm (pink diamonds). (b)The real-time cellular uptake data of PLGA nanoparticles with a diameter of 97 ± 3 nm from ref 11. Both are accurately described by eq A10 in this model. The results were obtained using the parameter values of k_a = 1.196 min^{-1} and k_r = 0.34 min^{-1} and summarized in 1b,d.

CONCLUSION

We have developed a deterministic kinetic model for endocytosis and proposed a clustering mechanism to describe nanoparticles smaller than the predicted energy cutoff aggregate on the cell surface after a 2D diffusion process in order to be endocytosed. The model is validated for DNA-wrapped single walled carbon nanotubes of lengths from 130 ± 18 to 660 ± 40 nm and for Au nanoparticles of diameters from 14 to 100 nm. This model describes the geometric influence and the dynamics of nanoparticle uptake for the first time. Both SWNT and Au have a maximum endocytosis rate near the 25 nm radius when scaled to account for diffusive interactions. The recycling (exocytosis) rate constants are similar in magnitude (10^{-4} to 10^{-3} min^{-1}) for poly((D,L-lactide-*co*-glycolide), SWNT, and Au nanoparti-

cles and decrease with increasing size of either the nanoparticle or its clusters. Therefore, the model is able to quantitatively predict the cellular uptake of nanoparticles, which is necessary for engineering nanosystems of controlled toxicity, efficacy, and functionality.

METHODS

Length Separation of Sodium Deoxycholate-SWNT. Single-walled HiPco carbon nanotubes (Rice University) were suspended with 2 wt % sodium deoxycholate surfactant (Sigma) with a SWNT concentration of 100 mg/L. The sample was sonicated with a probe tip sonicator in an ice water bath at 9W for 2 h. Each suspension was centrifuged at 21000*g* for 2 h to get individually dispersed SWNT. Using the technique in a recent paper,[44] SWNTs are length separated using density gradients and ultracentrifugation.

Resuspension of Sodium Deoxycholate-SWNT in DNA. Length fractions of sodium deoxycholate-SWNT were collected and then flocked using methanol. The flocked SWNTs were then washed with water (nanopure) several times to get rid of the surfactant and iodixanol used in the density gradient in the ultracentrifugation step. Finally, an extra 3 day dialysis against water (nanopure) using 12−14 kDa molecular weight cutoff dialysis tubing (Spectrum Laboratories Inc., Rancho Dominguez, CA) with three water changes per day was performed to ensure that all the surfactant and iodixanol were removed.

The length-separated SWNTs were then resuspended in a 30-based $d(GT)_{15}$ (Biotechnology Center, University of Illinois-Urbana−Champaign) with a 1:4 mass ratio in 0.1 M NaCl in distilled water and bath sonicated for 1 h. The mixture was then ultracentrifuged for 4 h at 30000 rpm (100000*g*) and the pellet discarded, yielding individually dispersed DNA-SWNTs.

Length Characterization by Atomic Force Microscope (AFM). Dimension 3100 (Digital Instruments) was used for AFM imaging. Samples were prepared by depositing a solution of $d(GT)_{15}$-SWNT(5 mg/L) on thermally oxidized silicon wafer (600 nm SiO_2, Montco Silicon Technologies). SWNT solution of 20 μL was drop dried on the cleaved wafer (30 mm × 30 mm) followed by rinsing with copious amount of nanopure water. Both topographic and height images were recorded during AFM anaysis. The length of the individual (unbundled) nanotubes was measured using the Digitial Instruments (DI) software. An example AFM image of each length used in this study is shown in Supporting Information, Figure S2a. The histogram for each length is shown in Figure S2b.

Fluorescence Microscopy for SPT. NIH3T3 fibroblast cells (ATCC) were cultured sparsely at 1.4×10^{-4} cells/μm^2 in DMEM (25 mM HEPES, 10% FBS and pen-strep) at 37 °C with a 5% CO_2 in a glass bottom 35 mm Petri dish (MatTek Corp., P35G-1.5−14-C). The Petri dish was then put in a microincubation platform (Model DH-40i, Warner Instruments, Inc.) on a fluorescence microscope (Carl Zeiss, Axiovert 200), with one CCD camera (Carl Zeiss, ZxioCam MRm) and one InGaAs detector (Princeton Instrument, 7531−0001) attached. Two syringes, one containing media and the other containing 5 mg/L DNA-SWNT in media, were connected to a controller (PC-16, Bioscience Tools) in order to switch between the two solutions. The solutions were fed by a miniature perfusion pump (CFPS-1 Units, Bioscience Tools) into the Petri dish within the incubation stage where microscopy measurements were taken under 785 nm laser excitation (Figure S3). Waste media solutions were removed *via* a second perfusion pump. Real-time movies were taken using WinSpec data acquisition program (Princeton Instruments) and SPT were done using ImageJ and its ParticleTracker plugin.[35]

During a typical experiment, a steady flow of media is established followed by one pulse of perfused DNA-SWNT in media. Since a flow field is maintained throughout the entire experiment, particles that contact but are otherwise not adsorbed onto the membrane are rapidly washed away with a velocity commensurate with the perfusion field, in contrast to the portion that are actually adsorbed. Fresh media is also perfused continuously ensuring cell viability.

The depth of field is calculated for the 63× oil immersion objective (numerical aperture = 1.4) and assuming the wavelength is 1000 nm (a good assumption since we are using CoMoCAT nanotubes) using the equation by Shillaber.[45] The imaging plane is focused on the cell cross section. The 295 nm depth of field of the camera is much smaller than the 5−6 μm thickness expected for cultured 3T3 cells,[46] so the trajectories observed accurately reflect the SWNT behaviors only on the cell cross-section plane. We assume that uptake is equally probable from any part of the cell membrane exposed to SWNTs. By tracking one imaging plane, we are measuring a portion of the entire cell, which is then converted to the entire cell for all our modeling purposes.

Using image processing algorithms,[35] SWNT trajectories are tracked from the sequence of images. Figure S4 superimposes example endocytosis, exocytosis, and flow trajectories recorded in the near-IR onto the corresponding optical CCD image of four different cells. SWNT endocytosis and exocytosis trajectories are counted in real-time and the rates are plotted in Figure S4. The total uptake is plotted in Figure 5a. Accumulation is calculated by subtracting the total number of exocytosis trajectories from the endocytosis trajectories.

Modeling of the Dynamics of the Uptake. The parameters used in A11 are (130 nm) $\mu = 60$ min, $\sigma = 70{:}10{:}100$ min; (320 nm) $\mu = 100$ min, $\sigma = 70{:}10{:}100$ min; (430 nm) $\mu = 100$ min, $\sigma = 50{:}10{:}100$ min; (660 nm) $\mu = 20$ min, $\sigma = 80{:}10{:}200$ min.

Acknowledgment. M.S. Strano is appreciative of a Beckman Young Investigator Award and funding from the National Science Foundation. We thank S. McMasters of the School of Chemical Sciences Cell Media Facility at the University of Illinois for cell culture assistance. AFM analysis was carried out in the Center for Microanalysis of Materials, University of Illinois, which is partially supported by the U.S. Department of Energy under grant DEFG02-91-ER45439.

Supporting Information Available: Supporting figures of the geometries of the clusters, atomic force microscope (AFM) images of the nanotubes, the perfusion setup, and examples of endocytosis and exocytosis trajectories. This material is available free of charge *via* the Internet at http://pubs.acs.org.

APPENDIX

Size-Dependent Uptake Model for Nanoparticles. For a typical incubation experiment where nanoparticles are coincubated with a cell population at $t = 0$ (*t*: time), the equations can be written as (Figure 2a):

$$\frac{dL}{dt} = (-k_f L R_s + k_r C_s)(n/N)$$

$$\frac{dC_s}{dt} = k_f L R_s - (k_r + k_e) C_s + k_{rec} C_i$$

$$\frac{dC_i}{dt} = k_e C_s - k_{rec} C_i$$

Here, *n* represents the cell density (cells/L) and *N* represents Avogadro's number.

For convenience, parameters can be grouped and simplified:

$$\frac{dL}{dt} = (-k_a L + k_r c_s) \quad \text{(A4)}$$

$$\frac{dc_s}{dt} = k_a L - (k_r + k_e) c_s + k_{rec} c_i \quad \text{(A5)}$$

$$\frac{dc_i}{dt} = k_e c_s - k_{rec} c_i \quad \text{(A6)}$$

$$k_a = k_f R_{s0}(n/N) \quad \text{(A7)}$$

$$c_s = C_s(n/N) \quad \text{(A8)}$$

where

$$c_i = C_i(n/N) \quad \text{(A9)}$$

R_{s0} is the initial surface receptor density.

The solution by Laplace transform yields

$$c_i = \frac{k_a k_e L_0}{\lambda_+ \lambda_- (\lambda_+ - \lambda_-)}\left((\lambda_+ - \lambda_-) + \lambda_- e^{-\lambda_+ t} - \lambda_+ e^{-\lambda_- t}\right) \quad \text{(A10)}$$

where

$$\lambda_\pm = \frac{(k_r + k_e + k_a + k_{rec}) \pm \sqrt{(k_r + k_e + k_a + k_{rec})^2 - 4(k_r k_{rec} + k_a k_e + k_a k_{rec})}}{2}$$

For a typical perfusion experiment described in this work and previously,[4] the initial condition for $L(t)$ is approximately a diffusion-controlled Gaussian distribution[43] that, in practice, is asymmetric and represented as a summation of Gaussians. Equation A5 becomes

$$\frac{dc_s}{dt} = k_a L_0 \overline{N(\mu, \sigma^2)} - (k_r + k_e)c_s + k_{rec} c_i \quad \text{(A11)}$$

where $N(\mu,\sigma^2)$ is the transient, pseudo-Gaussian distribution of nanoparticles with a mean of μ and a variance of σ^2 that passes over the cell in the perfusion field. In this case, the numerical solution of eq A6 and A11 is most convenient for obtaining the profiles of c_i and c_s. Experimentally, investigators typically measure the nanoparticle uptake as a function of exposure time which is potentially a function of both the endocytosis and exocytosis rates. Hence, the above model can be utilized to estimate rate constants for nanoparticle uptake for comparisons of nanoparticle uptake between various particle geometries and composition.

By this definition, the endocytosis rate constant, k_e, is predicted by the previous model derived by Gao and co-workers.[23]

REFERENCES AND NOTES

1. Chithrani, B. D.; Ghazani, A. A.; Chan, W. C. W. Determining the Size and Shape Dependence of Gold Nanoparticle Uptake into Mammalian Cells. *Nano Lett.* **2006**, *6*, 662–668.
2. Chithrani, B. D.; Chan, W. C. W. Elucidating the Mechanism of Cellular Uptake and Removal of Protein-Coated Gold Nanoparticles of Different Sizes and Shapes. *Nano Lett.* **2007**, *7*, 1542–1550.
3. Becker, M. L.; Fagan, J. A.; Gallant, N. D.; Bauer, B. J.; Bajpai, V.; Hobbie, E. K.; Lacerda, S. H.; Migler, K. B.; Jakupciak, J. P. Length-Dependent Uptake of DNA-Wrapped Single-Walled Carbon Nanotubes. *Adv. Mater.* **2007**, *19*, 939–945.
4. Jin, H.; Heller, D. A.; Strano, M. S. Single-Particle Tracking of Endocytosis and Exocytosis of Single-Walled Carbon Nanotubes in NIH-3T3 Cells. *Nano Lett.* **2008**, *8*, 1577–1585.
5. Kam, N. W. S.; Dai, H. J. Carbon Nanotubes as Intracellular Protein Transporters: Generality and Biological Functionality. *J. Am. Chem. Soc.* **2005**, *127*, 6021–6026.
6. Kam, N. W. S.; Jessop, T. C.; Wender, P. A.; Dai, H. J. Nanotube Molecular Transporters: Internalization of Carbon Nanotube-Protein Conjugates into Mammalian Cells. *J. Am. Chem. Soc.* **2004**, *126*, 6850–6851.
7. Kam, N. W. S.; Liu, Z. A.; Dai, H. J. Carbon Nanotubes as Intracellular Transporters for Proteins and DNA: An Investigation of the Uptake Mechanism and Pathway. *Angew. Chem., Int. Ed.* **2006**, *45*, 577–581.
8. Bianco, A.; Kostarelos, K.; Prato, M. Applications of Carbon Nanotubes in Drug Delivery. *Curr. Opin. Chem. Biol.* **2005**, *9*, 674–679.
9. Pantarotto, D.; Briand, J. P.; Prato, M.; Bianco, A. Translocation of Bioactive Peptides across Cell Membranes by Carbon Nanotubes. *Chem. Commun.* **2004**, *1*, 16–17.
10. Pantarotto, D.; Singh, R.; McCarthy, D.; Erhardt, M.; Briand, J. P.; Prato, M.; Kostarelos, K.; Bianco, A. Functionalized Carbon Nanotubes for Plasmid DNA Gene Delivery. *Angew. Chem., Int. Ed.* **2004**, *43*, 5242–5246.
11. Panyam, J.; Labhasetwar, V. Dynamics of Endocytosis and Exocytosis of Poly((D,L-lactide-*co*-glycolide) Nanoparticles in Vascular Smooth Muscle Cells. *Pharm. Res.* **2003**, *20*, 212–220.
12. Heller, D. A.; Baik, S.; Eurell, T. E.; Strano, M. S. Single-Walled Carbon Nanotube Spectroscopy in Live Cells: Towards Long-Term Labels and Optical Sensors. *Adv. Mater.* **2005**, *17*, 2793–2799.
13. Heller, D. A.; Jeng, E. S.; Yeung, T. K.; Martinez, B. M.; Moll, A. E.; Gastala, J. B.; Strano, M. S. Optical Detection of DNA Conformational Polymorphism on Single-Walled Carbon Nanotubes. *Science* **2006**, *311*, 508–511.
14. Chavanpatil, M. D.; Khdair, A.; Panyam, J. Surfactant-Polymer Nanoparticles: A Novel Platform for Sustained and Enhanced Cellular Delivery of Water-Soluble Molecules. *Pharm. Res.* **2007**, *24*, 803–810.
15. Hirsch, L. R.; Stafford, R. J.; Bankson, J. A.; Sershen, S. R.; Rivera, B.; Price, R. E.; Hazle, J. D.; Halas, N. J.; West, J. L. Nanoshell-Mediated Near-Infrared Thermal Therapy of Tumors under Magnetic Resonance Guidance. *Proc. Natl. Acad. Sci. U.S.A.* **2003**, *100*, 13549–13554.
16. Chen, J.; Saeki, F.; Wiley, B. J.; Cang, H.; Cobb, M. J.; Li, Z. Y.; Au, L.; Zhang, H.; Kimmey, M. B.; Li, X. D.; *et al.* Gold Nanocages: Bioconjugation and Their Potential Use as Optical Imaging Contrast Agents. *Nano Lett.* **2005**, *5*, 473–477.
17. West, J. L.; Halas, N. J. Engineered Nanomaterials for Biophotonics Applications: Improving Sensing, Imaging, and Therapeutics. *Annu. Rev. Biomed. Eng.* **2003**, *5*, 285–292.
18. Shukla, S.; Priscilla, A.; Banerjee, M.; Bhonde, R. R.; Ghatak, J.; Satyam, P. V.; Sastry, M. Porous Gold Nanospheres by Controlled Transmetalation Reaction: A Novel Material for Application in Cell Imaging. *Chem. Mater.* **2005**, *17*, 5000–5005.
19. Penn, S. G.; He, L.; Natan, M. J. Nanoparticles for Bioanalysis. *Curr. Opin. Chem. Biol.* **2003**, *7*, 609–615.
20. Kirchhausen, T. Three Ways to Make a Vesicle. *Nat. Rev. Mol. Cell Biol.* **2000**, *1*, 187–198.
21. Mukherjee, S.; Ghosh, R. N.; Maxfield, F. R. Endocytosis. *Physiol. Rev.* **1997**, *77*, 759–803.
22. Lynch, I. Are There Generic Mechanisms Governing Interactions between Nanoparticles and Cells? Epitope Mapping the Outer Layer of the Protein-Material Interface. *Phys. A* **2007**, *373*, 511–520.
23. Gao, H. J.; Shi, W. D.; Freund, L. B. Mechanics of Receptor-Mediated Endocytosis. *Proc. Natl. Acad. Sci. U.S.A.* **2005**, *102*, 9469–9474.
24. Freund, L. B.; Lin, Y. The Role of Binder Mobility in Spontaneous Adhesive Contact and Implications for Cell Adhesion. *J. Mech. Phys. Solids* **2004**, *52*, 2455–2472.
25. Decuzzi, P.; Ferrari, M. The Role of Specific and Non-Specific Interactions in Receptor-Mediated Endocytosis of Nanoparticles. *Biomaterials* **2007**, *28*, 2915–2922.
26. Decuzzi, P.; Ferrari, M. Design Maps for Nanoparticles Targeting the Diseased Microvasculature. *Biomaterials* **2008**, *29*, 377–384.
27. Lauffenburger, D. A.; Linderman, J. J. In *Receptors: Models for Binding, Trafficking, and Signaling*; Oxford University Press: New York, 1993; pp 30−95.

28. Tzafriri, A. R.; Wu, D.; Edelman, E. R. Analysis of Compartmental Models of Ligand-Induced Endocytosis. *J. Theor. Biol.* **2004**, *229*, 127–138.
29. Jiang, W.; Kim, B. Y. S.; Rutka, J. T.; Chan, W. C. W. Nanoparticle-Mediated Cellular Response Is Size-Dependent. *Nat. Nanotechnol.* **2008**, *3*, 145–150.
30. Jin, H.; Jeng, E. S.; Heller, D. A.; Jena, P. V.; Kirmse, R.; Langowski, J.; Strano, M. S. Divalent Ion and Thermally Induced DNA Conformational Polymorphism on Single-Walled Carbon Nanotubes. *Macromolecules* **2007**, *40*, 6731–6739.
31. Heller, D. A.; Mayrhofer, R. M.; Baik, S.; Grinkova, Y. V.; Usrey, M. L.; Strano, M. S. Concomitant Length and Diameter Separation of Single-Walled Carbon Nanotubes. *J. Am. Chem. Soc.* **2004**, *126*, 14567–14573.
32. Zheng, M.; Jagota, A.; Semke, E. D.; Diner, B. A.; McLean, R. S.; Lustig, S. R.; Richardson, R. E.; Tassi, N. G. DNA-Assisted Dispersion and Separation of Carbon Nanotubes. *Nat. Mater.* **2003**, *2*, 338–342.
33. Zheng, M.; Jagota, A.; Strano, M. S.; Santos, A. P.; Barone, P.; Chou, S. G.; Diner, B. A.; Dresselhaus, M. S.; McLean, R. S.; Onoa, G. B.; *et al*. Structure-Based Carbon Nanotube Sorting by Sequence-Dependent DNA Assembly. *Science* **2003**, *302*, 1545–1548.
34. The normalized photoluminescence intensity values used to correct for the quantum yield dependence on length in Figure 1 panels a, b, c, and d are 0.22, 0.82, 1.00, and 0.55, respectively.
35. Sbalzarini, I. F.; Koumoutsakos, P. Feature Point Tracking and Trajectory Analysis for Video Imaging in Cell Biology. *J. Struct. Biol.* **2005**, *151*, 182–195.
36. Berg, O. G.; Vonhippel, P. H. Diffusion-Controlled Macromolecular Interactions. *Annu. Rev. Biophys. Biophys. Chem.* **1985**, *14*, 131–160.
37. Freeman, D. L.; Doll, J. D. The Influence of Diffusion on Surface-Reaction Kinetics. *J. Chem. Phys.* **1983**, *78*, 6002–6009.
38. Richter, P. H.; Eigen, M. Diffusion Controlled Reaction Rates in Spheroidal Geometry: Application to Repressor-Operator Association and Membrane Bound Enzymes. *Biophys. Chem.* **1974**, *2*, 255–263.
39. Qian, Z. M.; Li, H.; Sun, H.; Ho, K. Targeted Drug Delivery *via* the Transferrin Receptor-Mediated Endocytosis Pathway. *Pharm. Rev* **2002**, *54*, 561–587.
40. Miller, K.; Shipman, M.; Trowbridge, I. S.; Hopkins, C. R. Transferrin Receptors Promote the Formation of Clathrin Lattices. *Cell* **1991**, *65*, 621–632.
41. Mashl, R. J.; Bruinsma, R. F. Spontaneous-Curvature Theory of Clathrin-Coated Membranes. *Biophys. J.* **1998**, *74*, 2862–2875.
42. Murray, R. K.; Granner, D. K.; Mayes, P. A.; Rodwell, V. W. *Harper's Biochemistry*; Appleton & Lange: Norwalk, CT, 1993.
43. Gaussian/normal distribution is chosen to characterize the concentration change of SWNT in our perfusion experiment because the change is diffusion-controlled and is continuous. Other distributions, like Boltzmann distribution, are more often used in quantum physics where there are obviously different states. For our system, we injected SWNTs into a perfusion chamber, and the SWNT is further diluted by the injected media. The concentration change should be continuous, and no distinct states should be expected. Hence it is better described by the Gaussian distribution.
44. Fagan, J. A.; Becker, M. L.; Chun, J.; Hobbie, E. K. Length Fractionation of Carbon Nanotubes Using Centrifugation. *Adv. Mater.* **2008**, *20*, 1609–1613.
45. Shillaber, C. P. In *Photomicrography in Theory and Practice*; John Wiley and Sons: New York, 1944; p 254.
46. Dorschel, B.; Hermsdorf, D.; Pieck, S.; Starke, S.; Thiele, H. Thickness Measurements on Cell Monolayers Using Cr-39 Detectors. *Nucl. Instrum. Methods Phys. Res., Sect. B* **2002**, *187*, 525–534.